Reversible collisionless magnetic reconnection

A. Ishizawa and T.-H. Watanabe

Citation: Physics of Plasmas (1994-present) **20**, 102116 (2013); doi: 10.1063/1.4826201
View online: http://dx.doi.org/10.1063/1.4826201
View Table of Contents: http://scitation.aip.org/content/aip/journal/pop/20/10?ver=pdfcov
Published by the AIP Publishing

Re-register for Table of Content Alerts

Create a profile. Sign up today!

This article is copyrighted as indicated in the abstract. Reuse of AIP content is subject to the terms at: http://scitation.aip.org/termsconditions. Downloaded to IP: 133.75.110.204 On: Tue, 12 Nov 2013 06:32:18

Reversible collisionless magnetic reconnection

A. Ishizawa and T.-H. Watanabe
National Institute for Fusion Science, Toki 509-5292, Japan

(Received 22 June 2013; accepted 25 September 2013; published online 18 October 2013)

Reversible magnetic reconnection is demonstrated for the first time by means of gyrokinetic numerical simulations of a collisionless magnetized plasma. Growth of a current-driven instability in a sheared magnetic field is accompanied by magnetic reconnection due to electron inertia effects. Following the instability growth, the collisionless reconnection is accelerated with development of a cross-shaped structure of current density, and then all field lines are reconnected. The fully reconnected state is followed by the secondary reconnection resulting in a weakly turbulent state. A time-reversed simulation starting from the turbulent state manifests that the collisionless reconnection process proceeds inversely leading to the initial state. During the reversed reconnection, the kinetic energy is reconverted into the original magnetic field energy. In order to understand the stability of reversed process, an external perturbation is added to the fully reconnected state, and it is found that the accelerated reconnection is reversible when the deviation of the E × B streamlines due to the perturbation is comparable with or smaller than a current layer width. © *2013 AIP Publishing LLC*. [http://dx.doi.org/10.1063/1.4826201]

I. INTRODUCTION

Magnetic reconnection is considered to be a key mechanism causing conversion of magnetic energy into kinetic energy in laboratory and space plasmas.[1] In magnetic fusion and solar corona, plasmas are subjected to an ambient magnetic field (so-called guide field) and are strongly magnetized. Magnetic reconnection in the magnetized plasma has been extensively studied by means of fluid models.[2–9] The fluid simulations of a current-driven instability revealed that the magnetic reconnection caused by electron inertia effects is accelerated by the gradient of perturbed electron pressure around the reconnection point.[2] However, plasmas in high-temperature magnetic fusion experiments and in solar corona are almost collisionless. A number of full-particle simulations have been carried out to study the collisionless magnetic reconnection without the guide field (see, for example, Refs. [10] and [11]). On the other hand, when plasmas are strongly magnetized, the gyrokinetic equation is useful for describing a collective motion of charged particles in a longer time-scale than the gyro-motions.[12,13] While the gyrokinetics is originally applied to drift waves and turbulence in magnetically confined plasmas, it is recently employed for studying the magnetic reconnection in strongly magnetized plasmas,[14,15] where the subsequent acceleration of reconnection is also found in the gyrokinetic simulation.[14]

As the fluid and kinetic equations in the collisionless limit are time-reversal invariant, the magnetic reconnection process, i.e., the transfer from magnetic to kinetic energy, is reversible in principle. However, it has not been shown in practice. If time-reversible reconnection is possible, then the kinetic energy produced by the magnetic reconnection could be transformed back into the magnetic energy. Studying the property of collisionless magnetic reconnection may help to understand a detailed mechanism of the sawtooth crash in the toroidal magnetic fusion experiments, where the $q = 1$ surface (q means the safety factor) is often recovered after the crash.[16] The study may also be helpful for understanding magnetic perturbations which may affect zonal flows regulating turbulent transport.[17]

In this paper, the reversibility of magnetic reconnection is investigated by means of collisionless gyrokinetic simulations. In the simulation, first, the collisionless magnetic reconnection develops in a sheared magnetic field, leading to a fully reconnected state (where all field lines are reconnected). The fully reconnected state is followed by the secondary reconnection leading to a weakly turbulent state. Next, we reverse the time in the simulation. It is found that the reconnection starting from the turbulent state proceeds inversely so that the field configuration returns to the initial state. The reversed process shows that the kinetic energy of plasmas is transformed back into the magnetic field one. The stability of the time-reversed reconnection is also examined.

The paper is organized as follows. In Sec. II, the gyrokinetic model used in this paper is described. In Sec. III, time-forwarded reconnection process is presented. Time-reversed reconnection is demonstrated in Sec. IV. In Sec. V, stability of reversed reconnection is examined. Summary and discussion are given in Sec. VI.

II. ELECTROMAGNETIC GYROKINETIC EQUATIONS

The gyrokinetic model in a slab plasma with uniform magnetic field in z direction (so-called guide field) is considered below. We assume uniform temperature and density profiles, and divide the distribution function into the Maxwellian and a perturbed part, $F_s = F_{Ms} + \delta f_s$, where $\delta f_s = \sum_k \delta f_{sk} \exp(i\mathbf{k}\cdot\mathbf{x})$. Here $\mathbf{k} = (k_x, k_y)$, and the subscript s denotes particle species. The gyrokinetic equation is

$$\frac{\partial \delta f_{sk}}{\partial t} - a_s v_\parallel \frac{q_s}{\tau_s} F_{Ms} E_{\parallel sk} + [(\phi - a_s v_\parallel A_\parallel) J_{0s}, \delta f_s]_k = 0, \quad (1)$$

and the gyrokinetic Poisson and Ampère equations are

 © 2013 AIP Publishing LLC

This article is copyrighted as indicated in the abstract. Reuse of AIP content is subject to the terms at: http://scitation.aip.org/termsconditions. Downloaded to IP: 133.75.110.204 On: Tue, 12 Nov 2013 06:32:18

$$\hat{\lambda}_{Di}^2 k^2 \phi_k = \sum_s q_s (\bar{n}_{sk} - \frac{q_s}{\tau_s}(1-\Gamma_{0s})\phi_k), \tag{2}$$

$$k^2 A_{\parallel k} = \beta_i \sum_s q_s \bar{u}_{\parallel sk}, \tag{3}$$

where $E_{\parallel sk} = -\frac{\partial A_{\parallel k}}{\partial t} J_{0s} - [\phi J_{0s}, A_\parallel J_{0s}]_k$, $[f,g]_k = -\sum_{k',k''} \delta_{k,k'+k''} \mathbf{b}\cdot\mathbf{k}'\times\mathbf{k}'' f_{k'} g_{k''}$, $\bar{n}_{sk} = \int \delta f_{sk} J_{0s} d^3v$, $\bar{u}_{\parallel sk} = \int a_s v_\parallel \delta f_{sk} J_{0s} d^3v$, $q_i = 1$, $q_e = -1$, and $\beta_i = n_0 T_i / B_0^2$. The normalizations are $(tv_{Ti}/L,\ k\rho_i,\ v_\parallel/v_{Ts},\ F_{Ms} v_{Ts}^3/n_0,\ \delta f_s L v_{Ts}^3/(\rho_i n_0),\ \phi e L/(\rho_i T_i),\ A_\parallel L/(B_0\rho_i^2),\ B/B_0) \to (t,\ k,\ v_z,\ F_{Ms},\ \delta f_s,\ \phi,\ A_\parallel,\ B)$, and $a_s = \sqrt{\tau_s/M_s}$, $\hat{\rho}_s = \rho_s/\rho_i$, $\hat{\lambda}_{Di} = \lambda_{Di}/\rho_i$, $q_s = e_s/e$, where $M_s = m_s/m_i$, $\tau_s = T_s/T_i$, $\rho_s = v_{Ts}/\Omega_s$, $\lambda_{Di} = \sqrt{T_i/(4\pi e^2 n_0)}$. In Eq. (2), $\Gamma_{0s} = e^{-b_{sk}} I_0(b_{sk})$, $b_{sk} = \hat{\rho}_s^2 k^2$, where I_0 is the zeroth order modified Bessel function and $J_{0s}(\rho_s k)$ is the zeroth order Bessel function. When the parallel electric field measured at gyro-center vanishes $E_{\parallel sk} = 0$, $A_\parallel J_{0s}$ obeys the same equation as δf_{sk}, so that the gyro-center magnetic flux moves in the same way as the gyro-center of particles. This implies the frozen-in of the gyro-center magnetic field to each species. Candidates of scale-lengths characterizing a reconnection region are the electron skin depth d_e, the ion and electron Larmor radius, ρ_i and ρ_e, respectively. The gyrokinetic equations Eqs. (1)–(3) are invariant under time-reversal, $t \to -t$ with $v_\parallel \to -v_\parallel$, and $(\phi, u_\parallel, A_\parallel, \mathbf{b}, [,]) \to (\phi, -u_\parallel, -A_\parallel, -\mathbf{b}, -[,])$. Conservation of a quadratic quantity is obtained from Eqs. (1)–(3), such that,

$$\frac{dH}{dt} = 0, \tag{4}$$

where $H = \sum_s S_s + W_{es} + W_{em}$,

$$S_s = \sum_k \int d^3v \frac{\tau_s |\delta f_{sk}|^2}{2F_{Ms}}, \tag{5}$$

$$W_{es} = \sum_k \left(\hat{\lambda}_{Di}^2 k^2 + \sum_s \frac{q_s^2}{\tau_s}(1-\Gamma_{0s}) \right) \frac{|\phi_k|^2}{2}, \tag{6}$$

and

$$W_{em} = \sum_k k^2 \frac{|A_{\parallel k}|^2}{2\beta_i}. \tag{7}$$

By using a modified distribution function $\delta f_{sk}^h = \delta f_{sk} + \frac{q_s}{\tau_s} F_{Ms} J_{0s} a_s v_\parallel A_{\parallel k}$, the gyrokinetic equation is rewritten in an advection form

$$\frac{\partial \delta f_{sk}^h}{\partial t} + [(\phi - a_s v_\parallel A_\parallel) J_{0s}, \delta f_s^h]_k = 0, \tag{8}$$

and conservation of a quadratic quantity is also derived for a fixed value of $v_\parallel$, $\frac{\partial}{\partial t}\sum_k |\delta f_{sk}^h|^2 = 0$. In addition, $\sum_k (\phi_k - a_s v_\parallel A_\parallel)^* J_{0s} \frac{\partial}{\partial t} \delta f_{sk}^h + \sum_k (\phi_k - a_s v_\parallel A_\parallel) J_{0s} \frac{\partial}{\partial t} \delta f_{sk}^{h*} = 0$ is obtained from Eq. (8). Thus, we recover $dH/dt = 0$, by adding these equations, rewriting δf_{sk}^h in terms of δf_{sk}, integrating over velocity space, summing over species, and using Eqs. (2) and (3). In our simulation, we further reduce the equation by assuming the Maxwellian gyro-center distribution function for the velocity component perpendicular to the guide field $\delta f_{sk} = f_{sk}(v_\parallel) F_{Ms\perp}$ and integrating Eq. (8) over $v_\perp$. Then, we have

$$\frac{\partial f_{sk}^h}{\partial t} + [(\phi - a_s v_\parallel A_\parallel) e^{-b_s/2}, f_s^h]_k = 0, \tag{9}$$

where $F_{Ms\perp} = \frac{1}{2\pi}\exp(-\frac{v_x^2+v_y^2}{2})$, $F_{Ms\parallel} = \frac{1}{(2\pi)^{1/2}}\exp(-\frac{v_\parallel^2}{2})$, and $F_{Ms} = F_{Ms\parallel} F_{Ms\perp}$. In the electrostatic limit $\beta_i \to 0$, the model is reduced to that in Ref. 18, and further simplified to that in Ref. 19 by assuming the adiabatic electron response. It is noticed that the zeroth order Bessel function $J_{0s}(\rho_s k)$ in the original gyrokinetic equation is replaced to $e^{-b_{sk}/2}$ by integrating over $v_\perp = \sqrt{v_x^2 + v_y^2}$ space. This introduces a strong damping effect due to the finite Larmor radius. Magnetic flux measured at gyro-center of each species is represented by $A_\parallel e^{-b_{sk}/2}$ and is called gyro-center magnetic flux in this paper.

A relation between the gyrokinetic model and a fluid one is briefly described below. Taking $v_\parallel$ integral of Eq. (9) multiplied by H_n leads to the fluid equation for the n-th order moment $G_{n,sk} = \int H_n(a_s v_\parallel) f_{sk}^h dv_\parallel$[20]

$$\frac{\partial G_{n,sk}}{\partial t} + [\Phi_s, G_{n,s}]_k - [\Psi_s, G_{n+1,s} + nG_{n-1,s}]_k = 0, \tag{10}$$

where H_n is the Hermite polynomials, $\Phi_{sk} = \phi_k e^{-b_{sk}/2}$, $\Psi_{sk} = A_{\parallel k} e^{-b_{sk}/2}$, $G_{0,sk} = n_{sk}$, $G_{1,sk} = u_{\parallel sk} + q_s \Psi_{sk} a_s^2/\tau_s$, $G_{2,sk} = T_{sk}$, and $G_{3,sk} = q_{\parallel sk}$. When the moment hierarchy is closed at the first order, i.e., $G_{n,s} = 0$ for $n \geq 2$, fluid equations for each species are obtained as

$$\frac{\partial n_{sk}}{\partial t} + [\Phi_s, n_s]_k - [\Psi_s, u_{\parallel s}]_k = 0, \tag{11}$$

$$\frac{\partial}{\partial t}\left(u_{\parallel sk} - q_s \frac{a_s^2}{\tau_s}\Psi_{sk} \right) + \left[\Phi_s, u_{\parallel s} - q_s \frac{a_s^2}{\tau_s}\Psi_s \right]_k - [\Psi_s, n_s]_k = 0. \tag{12}$$

In the long-wavelength limit of $\lambda_{Di} k < \rho_e k \ll \rho_i k < 1$, $e^{-b_{ek}/2} \simeq 1$, and $e^{-b_{ik}/2} \simeq 1/(1+b_{ik}/2)$, so that $\Phi_{ek} = \phi_k$, $\Phi_{ik} = \phi_k/(1+b_{ik}/2)$, $\Psi_{ek} = A_{\parallel k}$, and $\Psi_{ik} = A_{\parallel k}/(1+b_{ik}/2)$ in Eqs. (11) and (12), where the Poisson and Ampère equations, Eqs. (2) and (3), are reduced to

$$\frac{n_{ik}}{1+b_{ik}/2} - n_{ek} - \frac{1}{\tau_i}(1-\Gamma_{0i})\phi_k = 0, \tag{13}$$

and

$$k^2 A_{\parallel k} = \beta_i \left(\frac{u_{\parallel ik}}{1+b_{ik}/2} - u_{\parallel ek} \right), \tag{14}$$

respectively. Equations (11)–(14) are the same as Eqs. (2)–(8) in Ref. 8 except the normalizations, and S_s and W_{es} in H are replaced to $S_s \to \sum_k \frac{\tau_s}{2}(|n_{sk}|^2 + |u_{\parallel sk}|^2)$ and $W_{es} \to \sum_k \frac{1}{\tau_s}(1-\Gamma_{0i})\frac{|\phi_k|^2}{2}$, respectively. Equation (10) is time-reversal invariant, and thus the time-reversible magnetic reconnection shown in this paper should be obtained in

This article is copyrighted as indicated in the abstract. Reuse of AIP content is subject to the terms at: http://scitation.aip.org/termsconditions. Downloaded to IP: 133.75.110.204 On: Tue, 12 Nov 2013 06:32:18

fluid simulations as well, if sufficient numerical accuracy is ensured.

III. TIME-FORWARDED RECONNECTION

Numerical simulations of collisionless magnetic reconnection are carried out by solving the gyrokinetic equations, Eqs. (2), (3), and (9). The initial condition of f_{sk} is given by a sum of a very small perturbation and a shifted Maxwellian which produces a sheared magnetic field through the parallel current density. The simulation box size is $(L_x, L_y) = (2.5\pi\rho_i, 5\pi\rho_i)$. Numerical parameters are set to be $\beta_i = 0.02$, $m_i/m_e = 400$, and $T_i = T_e$. For these parameters, $\rho_e/\rho_i = \sqrt{m_e/m_i} = 1/20$ and $d_e/\rho_i = 1/\sqrt{8}$. The total number of Fourier modes for k_x and k_y is 512×512, and the number of grids in the $v_\parallel$ direction is 128.

Figure 1 shows the time evolution of magnetic field lines projected on the reconnection plane. Directions of an $E \times B$ flow are indicated by arrows in the frame at $t = 1140$. The magnetic reconnection takes place at $(x, y) = (L_x/2, L_y/2) = (1.25\pi\rho_i, 2.5\pi\rho_i)$. The plot of the magnetic field lines show that a separatrix angle between the y-axis and the field line passing through the reconnection point increases with the time from $t = 960$ to $t = 1200$. Change of the field configuration reflects a structural transition of a strong current density region around the reconnection point. A current sheet is formed along the y axis at $t = 960$, while it changes the form into a cross-shaped one as shown in Fig. 2. Streamlines of the $E \times B$ flow plotted at $t = 1080$ and 1140 in Fig. 3 indicate formation of a jet on the down-stream side of the reconnection point, which is accompanied with a converging in-flow. At $t = 1260$, most of the magnetic field lines are reconnected, and a fully reconnected state is formed.

Time evolutions of the $E \times B$ flow energy $k^2|\phi_k|^2/2$ and the magnetic energy $k^2|A_{\parallel k}|^2/(2\beta_i)$ for each Fourier mode of $k_y = 2\pi n/L_y$ are plotted in Fig. 4 (left). The initial growth of the $n = 1$ mode before $t = 1100$ is attributed to a current-driven instability with the magnetic reconnection caused by the electron inertia. Then, the growth of the $E \times B$ flow energy for $n = 1$ is accelerated around $t = 1170$, while the $n = 0$ magnetic energy decreases to a very small value. This suggests acceleration of the magnetic reconnection and a rapid change of the initial configuration with the sheared magnetic field. Accelerated growth of reconnection electric field, that is, $-\frac{\partial A_\parallel}{\partial t}(x = \frac{L_x}{2}, y = \frac{L_y}{2})$, is also shown in Fig. 5. The reconnection process around $t = 1170$ is referred to as accelerated reconnection in the followings. At this time, the form of the separatrix lines as well as the strong current density region is changed into the cross-shaped one as shown in Figs. 1 and 2. Then, the reconnection is completed around $t = 1230$. Figure 6 shows the current density profile on the horizontal line passing through the reconnection point at $y = L_y/2$. Width of the current density peak becomes narrow from the scale of d_e to ρ_e during the acceleration of reconnection around $t = 1170$.

Here, we discuss a time evolution subsequent to the fully reconnected state. A strong $E \times B$ flow induced at $t = 1200$ remains at $t = 1260$, as shown in Fig. 3, and convects magnetic field lines away from the reconnection point (see the plot at $t = 1260$ in Fig. 1). The $E \times B$ flow induces the secondary magnetic reconnection at $(x, y) = (L_x/2, 0)$ and $(L_x/2, L_y)$, which accompanies the current sheet elongated in the horizontal direction at $y = 0$ and L_y (see the plot at $t = 1260$ in Fig. 2). During the secondary reconnection, the kinetic energy is transformed back into the magnetic

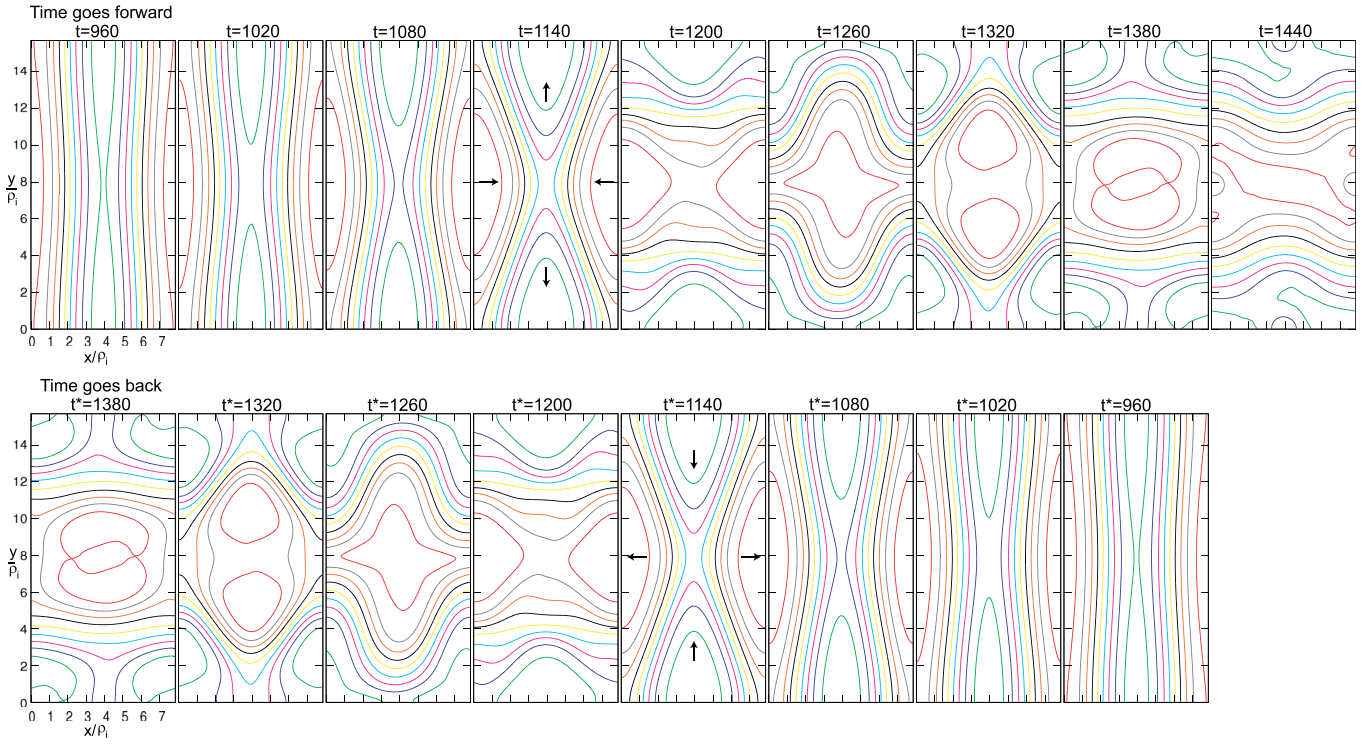

FIG. 1. Magnetic field lines projected on the reconnection plane. Time is reversed at $t = t^* = 1440$. When time goes forward (back), time is denoted by t (t^*) in the following figures. The arrows in the frames at $t = 1140$ and $t^* = 1140$ show the direction of $E \times B$ flow.

This article is copyrighted as indicated in the abstract. Reuse of AIP content is subject to the terms at: http://scitation.aip.org/termsconditions. Downloaded to IP: 133.75.110.204 On: Tue, 12 Nov 2013 06:32:18

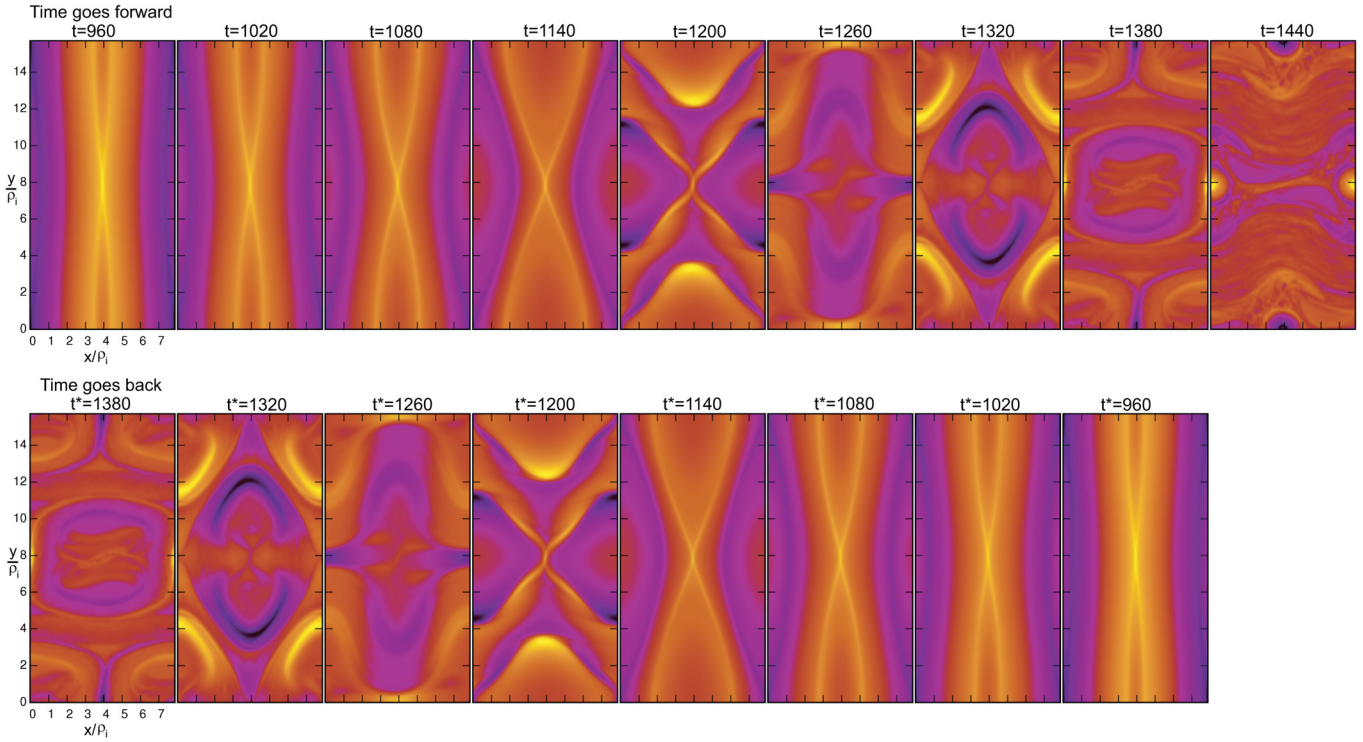

FIG. 2. Color-map of current density.

energy at $t = 1300$ as found in Fig. 4. As the secondary reconnection is a partial one, the magnetic energy is transformed back into kinetic energy at $t = 1400$. If the secondary reconnection could proceed more, the initial vertical magnetic field line configuration might be recovered. But, it ends before $t = 1320$ and results in formation of magnetic islands (see plots at $t = 1320$ and 1380 in Fig. 1). Eventually, most of the magnetic field lines become horizontal at $t = 1440$ as found in Fig. 1, where the $E \times B$ flow shown in Fig. 3 is weakly turbulent. Turbulent fluctuations are also observed in the current density profile at $t = 1440$ (see Fig. 2), especially, in weak magnetic field regions. While the system does not reach a completely steady state even after $t = 1440$, the magnetic field lines remain horizontal but with small oscillations.

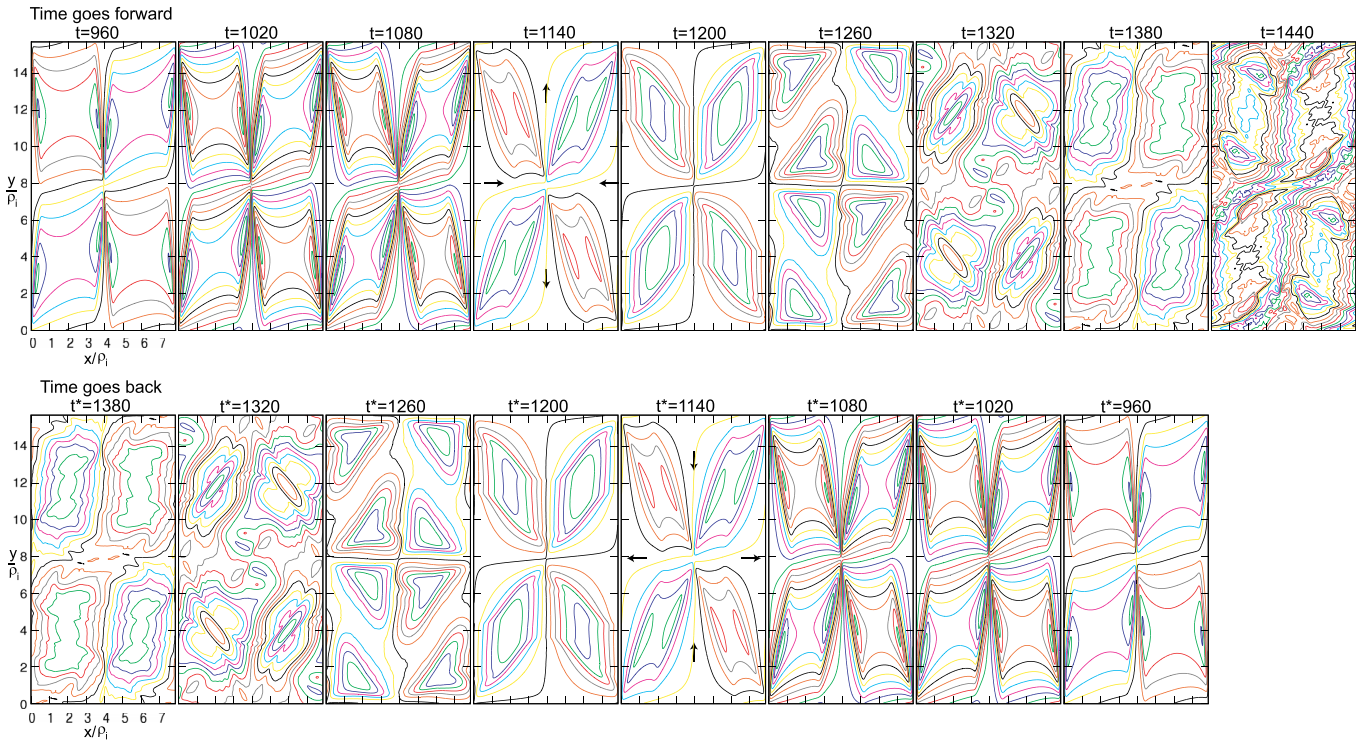

FIG. 3. Stream lines of $E \times B$ flow.

This article is copyrighted as indicated in the abstract. Reuse of AIP content is subject to the terms at: http://scitation.aip.org/termsconditions. Downloaded to IP: 133.75.110.204 On: Tue, 12 Nov 2013 06:32:18

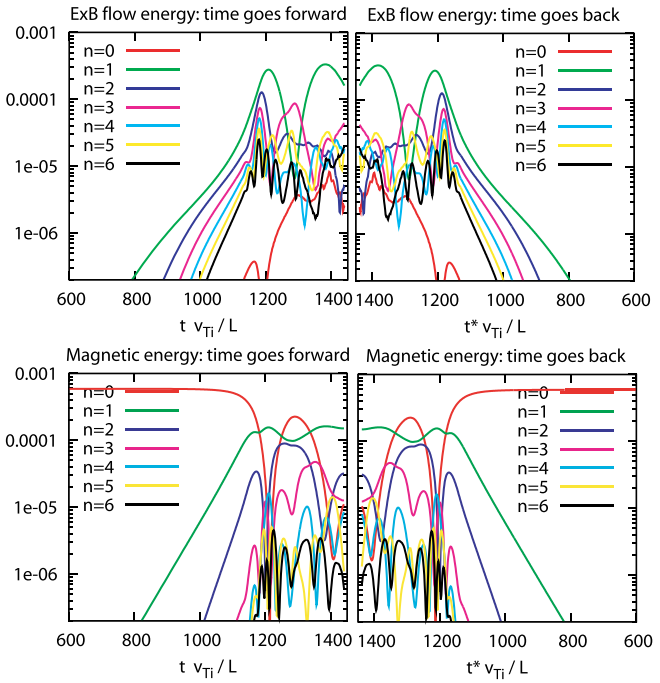

FIG. 4. Time evolution of $E \times B$ flow energy $k^2|\phi_k|^2/2$ and magnetic energy $k^2|A_{\|k}|^2/(2\beta_i)$ for each Fourier mode $k_y = 2\pi n/L_y$. When time goes forward (back), time is denoted by t (t^*).

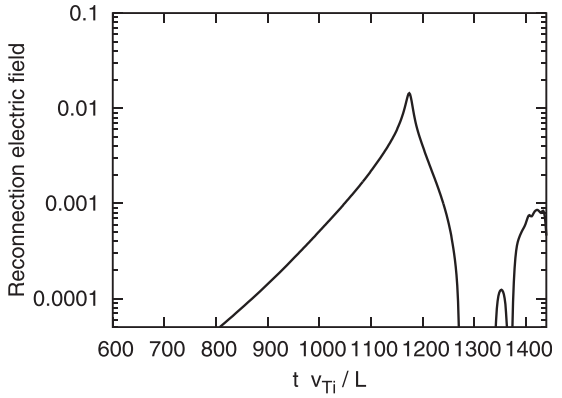

FIG. 5. Time evolution of reconnection electric field $-\frac{\partial A_\|}{\partial t}(x = \frac{L_x}{2}, y = \frac{L_y}{2})$.

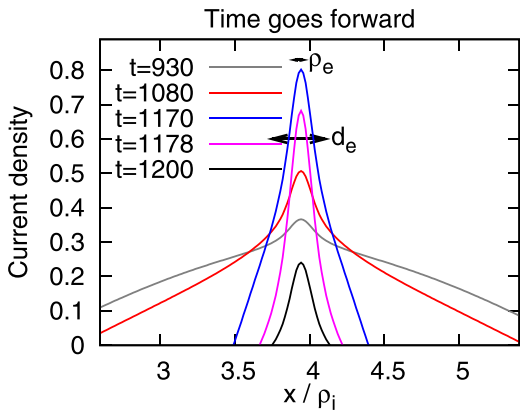

FIG. 6. Profile of current density along the horizontal line passing through the reconnection point $y = L_y/2$.

Thus, the horizontal magnetic field configuration at $t = 1440$ is an asymptotic state.

Here, we examine time evolutions of the quadratic quantities. Figure 7 shows the time histories of the conserved quantity $H = \sum_s S_s + W_{es} + W_{em}$ and each term constituting it. The numerical solution well satisfies the conservation equation in Eq. (4) with negligible numerical errors. The magnetic energy W_{em} is rapidly lost during the accelerated reconnection around $t = 1170$ and is transformed into W_{es} and S_e. This implies the magnetic energy is converted into the $E \times B$ flow and parallel kinetic energies thorough the magnetic reconnection. Although the $E \times B$ flow and the current density are weakly turbulent at $t = 1440$, the conservation of the quadratic quantity $dH/dt = 0$ is well satisfied.

Finally, we present deformation of the velocity distribution function during the magnetic reconnection. Figure 8(a) shows the electron distribution function f_e at the reconnection point $(x, y) = (L_x/2, L_y/2)$. The distribution function is given by the shifted-Maxwellian at $t = 0$, and then is deformed during the reconnection. A peak of the distribution is shifted to the negative $v_\|$ direction because the reconnection electric field is produced by the acceleration of electrons to $-v_\|$-direction at the reconnection point, i.e., the magnetic reconnection is caused by the electron inertia effect. In other words, the reconnection electric field accelerates the electrons to the parallel direction. Production of non-thermal particles is one of the interesting features of magnetic reconnection.[21] However, in this simulation, the deformation of f_e at large $v_\|$ is small, and thus the production of non-Maxwellian part, i.e., non-thermal part, is negligible as shown in Fig. 8(c).

The reconnection process described in this section is referred to as time-forwarded reconnection in the followings.

IV. TIME-REVERSED RECONNECTION

Here, we demonstrate that the magnetic reconnection process described Sec. III is time-reversible. The simulation described above is stopped at $t = 1440$ and the data are stored. Then, changing the sign of time-step width $\Delta t \to -\Delta t$ the simulation is restarted from the saved data which is used as the initial condition at $t^* = 1440$, where t^* denotes the time in the time-reversed simulation. Figures 1–3 show that profiles of the magnetic field lines, the current density and the $E \times B$ flow at $t^* = 1320$, 1200, 1080, and 960 are exactly the same as those at $t = 1320$, 1200, 1080, and 960 in the time-forwarded reconnection, respectively. Arrows in the plot of magnetic field lines at $t^* = 1140$ indicate the direction of reversed $E \times B$ flows. In the time-reversed reconnection, the magnetic field lines are convected in the opposite directions to those in the time-forwarded case and are reconnected so as to return to the initial configuration. The current density profile is also time-reversible, where the cross-shaped structure returns to the elongated one parallel to the y-axis. The $E \times B$ flow pattern also returns to the initial state observed in the time-forwarded reconnection.

Figure 4 (right) shows time evolutions of the $E \times B$ flow energy $k^2|\phi_k|^2/2$ and the magnetic energy $k^2|A_{\|k}|^2/(2\beta_i)$ for each Fourier mode in the time-reversed simulation from

This article is copyrighted as indicated in the abstract. Reuse of AIP content is subject to the terms at: http://scitation.aip.org/termsconditions. Downloaded to IP: 133.75.110.204 On: Tue, 12 Nov 2013 06:32:18

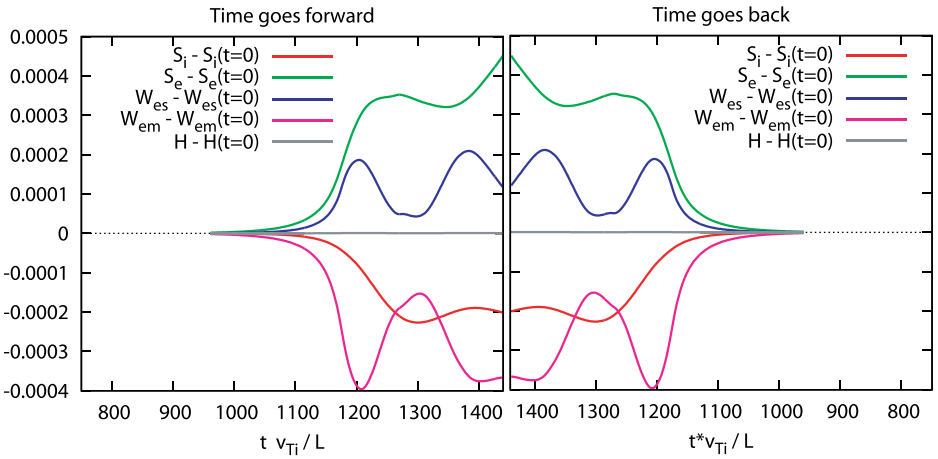

FIG. 7. Time evolution of the conserved quantity $H = \sum_s S_s + W_{es} + W_{em}$, and each term constituting it.

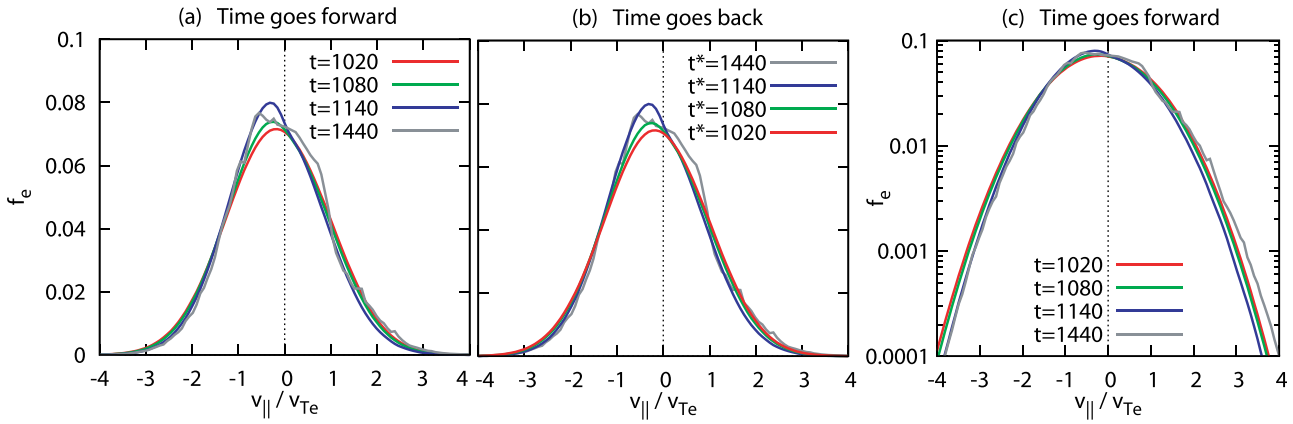

FIG. 8. Electron gyro-center distribution function f_e in the velocity space around the reconnection point $(x, y) = (L_x/2, L_y/2)$.

$t^* = 1440$ to $t^* = 600$, where each mode traces back the same line observed in the time-forwarded simulation. The result manifests that the magnetic reconnection process is reversed from the fully reconnected state to the initial state.

Deformation of the distribution function in the velocity space is also time-reversible as shown in Fig. 8(b), where the profile of f_e at each time in the time-reversed reconnection is the same as that in the time-forwarded reconnection. It means that the deformed distribution function in the velocity space goes back to the initial state of the time-forwarded reconnection. In our simulation, the magnetic reconnection is completed before fine velocity-space structures fully develop. If the velocity-space structure of f_e was finer than the grid size, the simulation was not reliable.

The recovery to the initial profile of f_e and the decrease in S_e in the reversed reconnection (Fig. 7) imply that the kinetic energy for the parallel velocity component is transformed back into the original magnetic field energy. Also, the E × B flow energy transformed from magnetic energy is reconverted into the magnetic energy as shown in Figs. 4 and 7.

V. STABILITY OF REVERSED RECONNECTION

In this section, stability of the time-reversed magnetic reconnection is examined by adding an external perturbation f_{err} to the distribution function in the fully reconnected state when the reversed reconnection simulation is started at $t^* = 1230$. Figure 9 shows sensitivity of the reversed reconnection on the perturbation amplitude. For very small perturbation of $\delta f_{err} \approx 10^{-8}$, the E × B flow energy, $k^2|\phi_k|^2/2$, for $n = 1$ Fourier mode traces back the history of the time-forwarded reconnection from $t^* = 1230$ to $t^* = 960$, where $\delta f_{err} = |f_{err}|/|f_s(t = 1230)|$. When the perturbation amplitude is increased to $\delta f_{err} \approx 10^{-3}$, the flow energy of the $n = 1$ mode evolves following the result of the time-forwarded reconnection until $t^* = 1140$, and then starts to deviate from it. Thus, the reversed reconnection is sensitive to amplitudes of the perturbation during the reconnection from $t^* = 1140$ to $t^* = 960$, when the initial growth of the current-driven instability was observed in the forwarded reconnection accompanied with the elongated current profile. On the other hand, the reversed reconnection around $t^* = 1170$, that corresponds to the accelerated reconnection around $t = 1170$ in the forwarded reconnection, is less sensitive to the perturbation amplitude. Figure 9 shows most of the magnetic energy $k^2|A_{||k}|^2/(2\beta_i)$ for $n = 1$ Fourier mode is recovered around $t^* = 1100$, in the case of $\delta f_{err} \leq 10^{-3}$ (but not for $\delta f_{err} \approx 10^{-2}$). It means most of the kinetic energy at $t^* = 1230$ is transformed into the magnetic energy at $t^* = 1100$ in the reversed reconnection. Figure 10 shows the time evolution of reconnected flux $A_{||}(L_x/2, L_y/2)$ and of reconnection electric field $-dA_{||}(L_x/2, L_y/2)/dt$, where most of the initial magnetic flux is recovered at $t^* = 1000$ for

This article is copyrighted as indicated in the abstract. Reuse of AIP content is subject to the terms at: http://scitation.aip.org/termsconditions. Downloaded to IP: 133.75.110.204 On: Tue, 12 Nov 2013 06:32:18

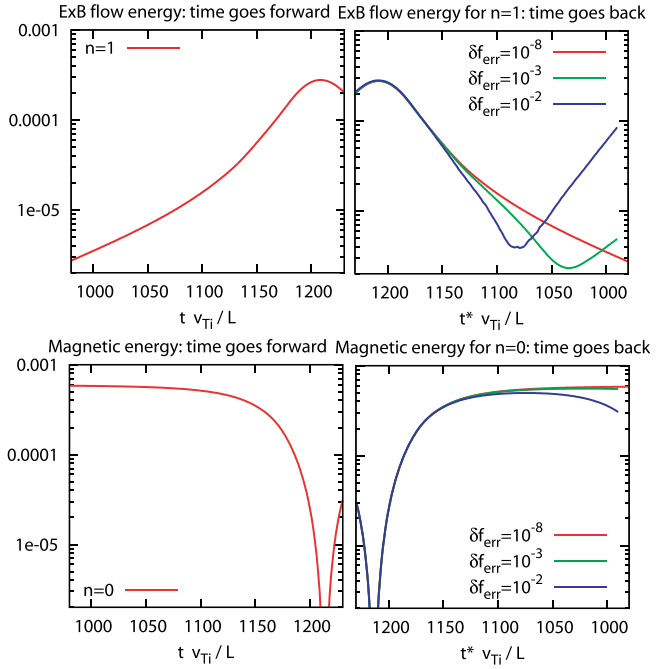

FIG. 9. Time evolution of $E \times B$ flow energy $k^2|\phi_k|^2/2$ for $n=1$ Fourier mode and magnetic energy $k^2|A_{\|k}|^2/(2\beta_i)$ for $n=0$ mode, where $k_y = 2\pi n/L_y$. A small perturbation δf_{err} is added when time is reversed $t = t^* = 1230$.

$\delta f_{err} \le 10^{-3}$. Even for $\delta f_{err} \approx 10^{-2}$, more than a half of the magnetic flux is reconnected during the reversed simulation. The reconnection electric field in the time-reversed case has a negative peak around $t^* = 1175$ and the peak amplitudes for $\delta f_{err} \le 10^{-3}$ are similar to that in the time-forwarded reconnection. The reconnection electric field for $\delta f_{err} \approx 10^{-2}$ is weaker than the time-forwarded case, and thus the accelerated reconnection is not reversible when the external perturbation is larger than $\delta f_{err} \approx 10^{-2}$.

Here, we investigate the detailed process, in which the system does not go back to the initial state because of the external perturbation. Figures 11–13, respectively, show the magnetic field lines, the current density and the $E \times B$ flow patterns at $t^* = 1170$ and 1140 in a magnified region around the reconnection point. In Fig. 11(a) for $\delta f_{err} \approx 10^{-8}$, the magnetic field line colored by red has been reconnected at $t^* = 1170$, while in Fig. 11(b) for $\delta f_{err} \approx 10^{-3}$, it is going to be reconnected at $t^* = 1170$. It means that the reconnection for the latter is slower than the former. The slowdown of reconnection in the case with $\delta f_{err} \approx 10^{-3}$ is also confirmed by the field line colored by black which has been reconnected for $\delta f_{err} \approx 10^{-8}$ at $t^* = 1140$ but not in the case of $\delta f_{err} \approx 10^{-3}$. It is much clearer for the case $\delta f_{err} \approx 10^{-2}$ and is associated with piling up of the magnetic flux in the upstream region of the reconnection point. Then, the flux pile-up prevents the system to go back to the initial state. The slowing down of the reconnection is also confirmed in the plots of the current density and the $E \times B$ flow.

As we have seen the reconnection is reversible for the very small external perturbation of $\delta f_{err} \approx 10^{-8}$. In the reversible reconnection, the current density has a peak at the reconnection point as shown in Fig. 12(a), and the $E \times B$ flow converges to the reconnection point from up and bottom sides of each panel [see Fig. 13(a)]. This converging flow corresponds to the reversal of the outward jet flow formed in the down-stream region of the reconnection point in the time-forwarded reconnection. For $\delta f_{err} \approx 10^{-3}$ shown in Fig. 13(b), the flow pattern is similar to that for $\delta f_{err} \approx 10^{-8}$ at $t^* = 1170$. Then, the $E \times B$ flow stagnates in the upstream of the reconnection point in Fig. 13(b) at $t^* = 1140$. As shown in Figs. 11(b) and 11(c) at $t^* = 1140$, the stagnation of flow causes the flux pile-up at the up-stream region, where the current density is more largely enhanced than that at the reconnection point as found in Figs. 12(b) and 12(c).

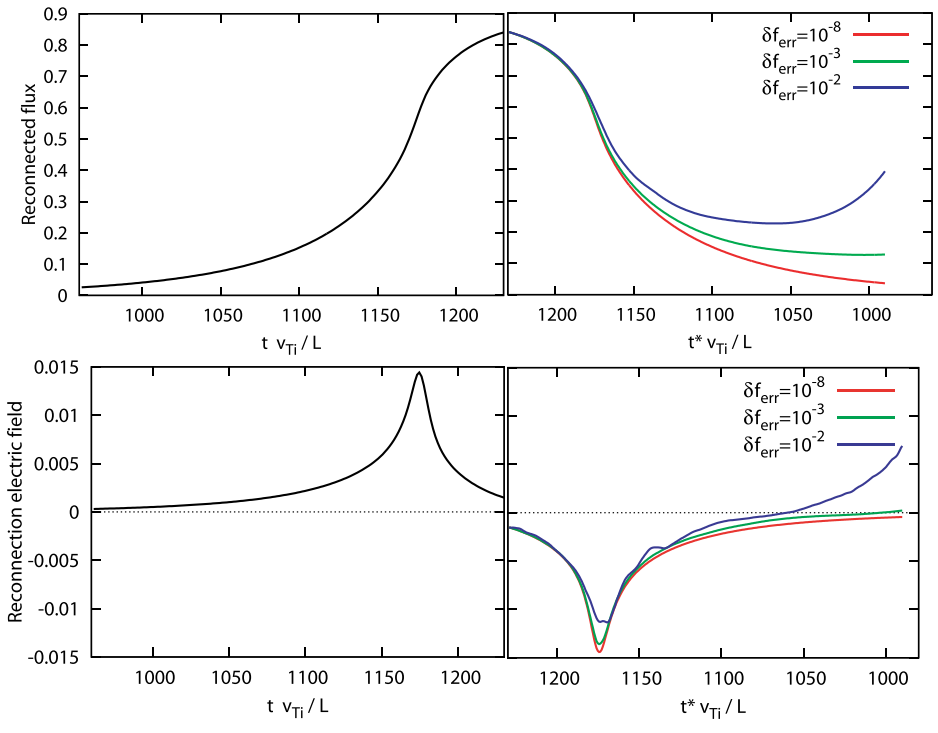

FIG. 10. Time evolution of reconnected flux $A_{\|}(L_x/2, L_y/2)$ and reconnection electric field $-dA_{\|}(L_x/2, L_y/2)/dt$ for small perturbation δf_{err} added when time is reversed $t = t^* = 1230$.

This article is copyrighted as indicated in the abstract. Reuse of AIP content is subject to the terms at: http://scitation.aip.org/termsconditions. Downloaded to IP: 133.75.110.204 On: Tue, 12 Nov 2013 06:32:18

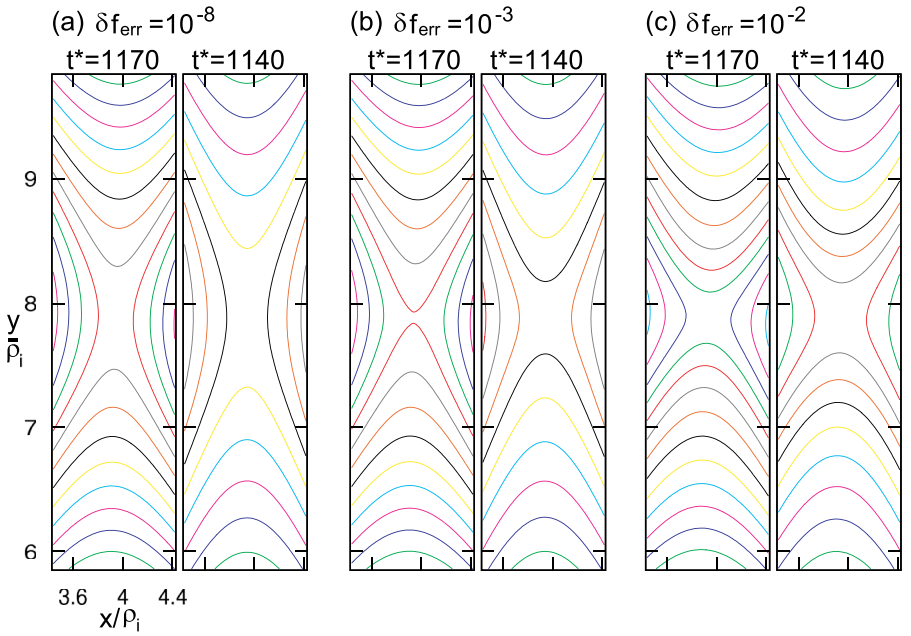

FIG. 11. Magnetic field lines in a region magnified around the reconnection point $(x, y) = (3.93\rho_i, 7.85\rho_i)$, when the external perturbation δf_{err} is added.

Figure 13(c) for $\delta f_{err} \approx 10^{-2}$ also shows that streamlines of the $E \times B$ flow towards the reconnection point significantly deviate from those in (a).

Finally, fluctuations of streamlines induced by the external perturbations are examined more in detail. Figure 14 shows the streamlines of the $E \times B$ flow towards the reconnection point in the accelerated phase of the time-reversed reconnection at $t^* = 1170$ for the cases of $\delta f_{err} \approx 10^{-8}$, 10^{-3}, and 10^{-2}. As the reconnection is completely reversible for $\delta f_{err} \approx 10^{-8}$, deviations from this line could be a measure for an error in the $E \times B$ convection of the magnetic field to the reconnection point. The accelerated reconnection is time-reversible when the perturbation is small ($\delta f_{err} \leq 10^{-3}$) as shown in Figs. 9 and 10. For the small perturbation of $\delta f_{err} \approx 10^{-3}$, deviation of the streamline is quite small ($\approx 0.05\rho_i$) and is comparable with the current layer width [see Fig. 12(a)] characterized by electron scales $d_e = \rho_i/\sqrt{8}$ and $\rho_e = \rho_i/20$. In contrast, the streamline largely fluctuates in the x-direction for the case of $\delta f_{err} \approx 10^{-2}$. The above results imply that the accelerated reconnection is reversible when the deviation of the $E \times B$ streamlines from those in the case without the perturbation is comparable with or smaller than the current layer width characterized by the electron scales.

VI. SUMMARY AND DISCUSSION

Time-reversible magnetic reconnection is demonstrated by means of the collisionless gyrokinetic simulations. First, we have presented the time-forwarded simulation starting from a sheared magnetic field with a small initial perturbation, where a current-driven instability grows with magnetic reconnection caused by electron inertia effects. The reconnection speed is accelerated when a cross-shaped structure

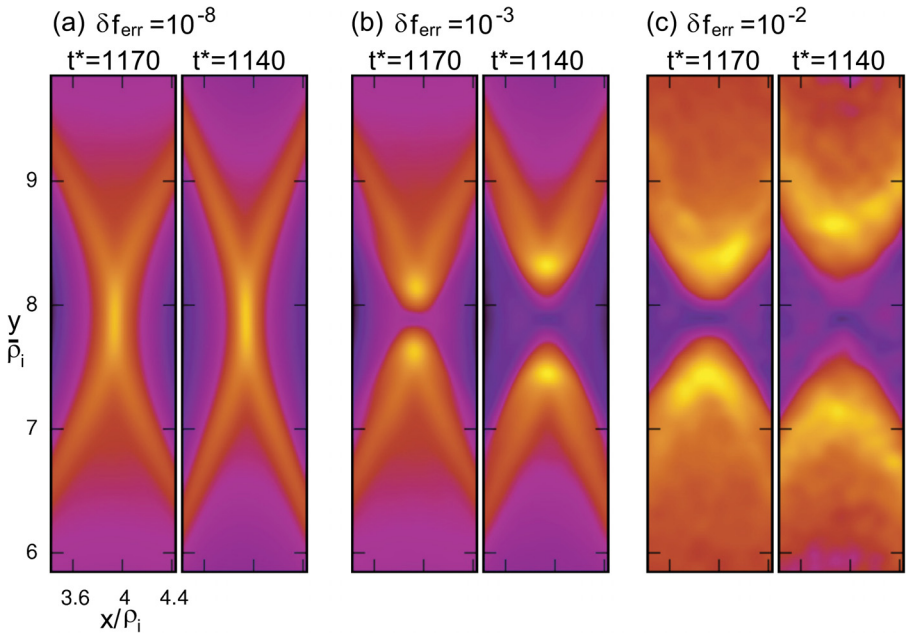

FIG. 12. Color-map of current density in a region magnified around the reconnection point $(x, y) = (3.93\rho_i, 7.85\rho_i)$, when the external perturbation δf_{err} is added.

This article is copyrighted as indicated in the abstract. Reuse of AIP content is subject to the terms at: http://scitation.aip.org/termsconditions. Downloaded to IP: 133.75.110.204 On: Tue, 12 Nov 2013 06:32:18

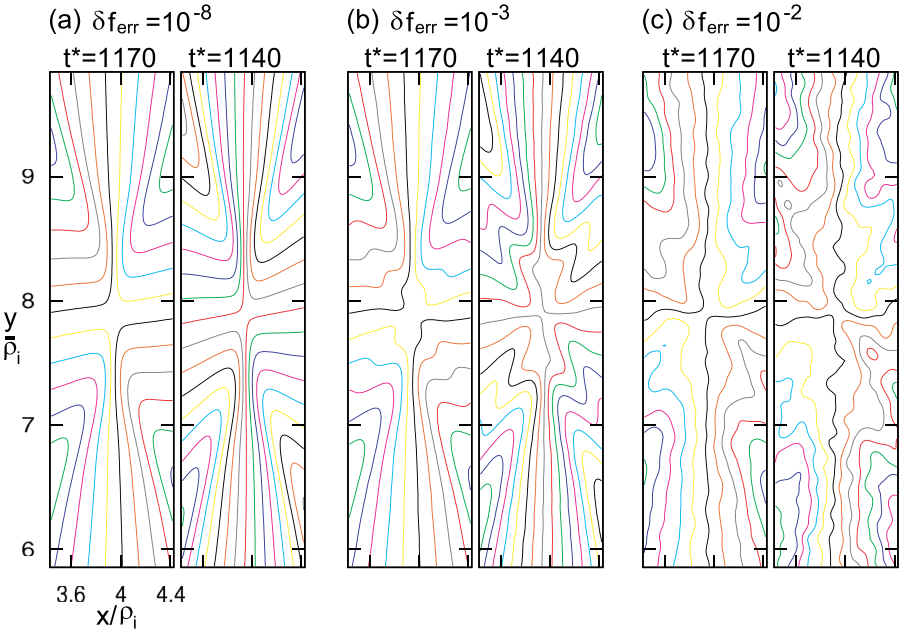

FIG. 13. Stream lines of $E \times B$ flow in a region magnified around the reconnection point $(x, y) = (3.93\rho_i, 7.85\rho_i)$, when the external perturbation δf_{err} is added.

of current density appears. Then, all field lines are reconnected. This process is similar to that observed in the previous numerical studies by fluid and gyrokinetic simulations.[2,14] Even in the fully reconnected state, a strong $E \times B$ flow remains and causes the secondary magnetic reconnection. Then, the system reaches a weakly turbulent state where a horizontal magnetic field normal to the initial field is dominant. In the weakly turbulent state following the fully reconnected one, we stopped the simulation, and stored the numerical data. Then, the time-reversed simulation is started from the saved data and by changing the time-step from Δt to $-\Delta t$, where the reconnection process described above is retraced. The reconnected magnetic field lines and the deformed distribution function in the velocity space return to their initial profiles in the time-reversed reconnection with reconversion of the kinetic energy to the magnetic one.

Stability of the time-reversed reconnection is examined by adding perturbations to the restart data used in the time-reversed simulation. The accelerated reconnection, which occurs before reaching the fully reconnected state in the time-forwarded simulation, is time-reversible with the transformation of the kinetic energy to the magnetic energy, when the perturbations are small. It is found that the deviation of an $E \times B$ flow streamlines through the reconnection region provides a measure of the threshold for the external perturbation preventing the reversible reconnection. When the deviation is comparable with or smaller than the current layer width, the accelerated reconnection with the cross-shaped current structure is reversible.

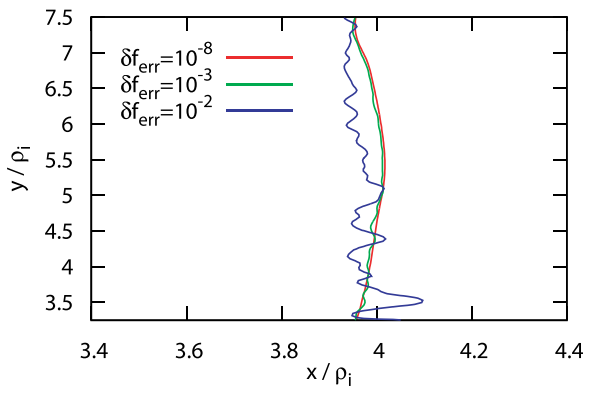

FIG. 14. The $E \times B$ flow streamline towards the reconnection point $(x, y) = (3.93\rho_i, 7.85\rho_i)$, when the external perturbation δf_{err} is added.

ACKNOWLEDGMENTS

Authors would like to thank Professor F. L. Waelbroeck for valuable discussions and also thank Professors R. Horiuchi and H. Sugama for their support. The work is supported by the Japanese Ministry of Education, Culture, Sports, Science and Technology, Grant No. 23561003.

[1]D. Biskamp, *Magnetic Reconnection in Plasmas* (Cambridge University Press, Cambridge, 2000).
[2]A. Y. Aydemir, Phys. Fluids B **4**, 3469 (1992).
[3]M. Ottaviani and F. Porcelli, Phys. Rev. Lett. **71**, 3802 (1993).
[4]D. Grasso, F. Califano, F. Pegoraro, and F. Porcelli, Phys. Rev. Lett. **86**, 5051 (2001).
[5]E. Tassi, P. J. Morrison, F. L. Waelbroeck, and D. Grasso, Plasma Phys. Controlled Fusion **50**, 085014 (2008).
[6]F. L. Waelbroeck, R. D. Hazeltine, and P. J. Morrison, Phys. Plasmas **16**, 032109 (2009).
[7]D. Grasso, E. Tassi, and F. L. Waelbroeck, Phys. Plasmas **17**, 082312 (2010).
[8]L. Comisso, D. Grasso, E. Tassi, and F. L. Waelbroeck, Phys. Plasmas **19**, 042103 (2012).
[9]M. Hirota, P. J. Morrison, Y. Ishii, M. Yagi, and N. Aiba, Nucl. Fusion **53**, 063024 (2013).
[10]R. Horiuchi and T. Sato, Phys. Plasmas **6**, 4565 (1999).
[11]J. Birn *et al.*, J. Geophys. Res. **106**, 3715, doi:10.1029/1999JA900449 (2001).
[12]E. A. Frieman and L. Chen, Phys. Fluids **25**, 502 (1982).
[13]T. S. Hahm, W. W. Lee, and A. Brizard, Phys. Fluids **31**, 1940 (1988).
[14]M. J. Pueschel, F. Jenko, D. Told, and J. Buchner, Phys. Plasmas **18**, 112102 (2011).
[15]R. Numata, W. Dorland, G. G. Howes *et al.*, Phys. Plasmas **18**, 112106 (2011).
[16]F. M. Levinton *et al.*, Phys. Fluids B **5**, 2554 (1993).

This article is copyrighted as indicated in the abstract. Reuse of AIP content is subject to the terms at: http://scitation.aip.org/termsconditions. Downloaded to IP: 133.75.110.204 On: Tue, 12 Nov 2013 06:32:18

[17]M. J. Pueschel *et al.*, Phys. Rev. Lett. **110**, 155005 (2013).
[18]A. Ishizawa, T.-H. Watanabe, and N. Nakajima, Plasma Fusion Res. **6**, 2403087 (2011).
[19]T.-H. Watanabe and H. Sugama, Phys. Plasmas **11**, 1476 (2004).
[20]H. Sugama, T.-H. Watanabe, and W. Horton, Phys. Plasmas **8**, 2617 (2001).
[21]M. Hoshino, T. Mukai, T. Terasawa, and I. Shinohara, J. Geophys. Res. **106**(A11), 25979, doi:10.1029/2001JA900052 (2001).

This article is copyrighted as indicated in the abstract. Reuse of AIP content is subject to the terms at: http://scitation.aip.org/termsconditions. Downloaded to IP: 133.75.110.204 On: Tue, 12 Nov 2013 06:32:18